

# Tuning the Anode–Electrolyte Interface Chemistry for Garnet-Based Solid-State Li Metal Batteries

Tao Deng, Xiao Ji, Yang Zhao, Longsheng Cao, Shuang Li, Sooyeon Hwang, Chao Luo, Pengfei Wang, Haiping Jia, Xiulin Fan, Xiaochuan Lu, Dong Su, Xueliang Sun, Chunsheng Wang,\* and Ji-Guang Zhang\*

Lithium (Li) metal is a promising candidate as the anode for high-energy-density solid-state batteries. However, interface issues, including large interfacial resistance and the generation of Li dendrites, have always frustrated the attempt to commercialize solid-state Li metal batteries (SSLBs). Here, it is reported that infusing garnet-type solid electrolytes (GSEs) with the air-stable electrolyte  $\text{Li}_3\text{PO}_4$  (LPO) dramatically reduces the interfacial resistance to  $\approx 1 \Omega \text{ cm}^2$  and achieves a high critical current density of  $2.2 \text{ mA cm}^{-2}$  under ambient conditions due to the enhanced interfacial stability to the Li metal anode. The coated and infused LPO electrolytes not only improve the mechanical strength and Li-ion conductivity of the grain boundaries, but also form a stable Li-ion conductive but electron-insulating LPO-derived solid-electrolyte interphase between the Li metal and the GSE. Consequently, the growth of Li dendrites is eliminated and the direct reduction of the GSE by Li metal over a long cycle life is prevented. This interface engineering approach together with grain-boundary modification on GSEs represents a promising strategy to revolutionize the anode–electrolyte interface chemistry for SSLBs and provides a new design strategy for other types of solid-state batteries.

The ever-increasing demand from electric vehicles and consumer electronics, as well as the expanding market of intermittent renewable energy storage, has sparked extensive research on energy-storage devices with low cost, high energy density, and safety.<sup>[1]</sup> Solid-state batteries (SSBs) using inorganic solid-state electrolytes (SSEs) are widely regarded as the next-generation energy storage system, which may replace the state-of-the-art Li-ion batteries with flammable organic electrolytes.<sup>[2,3]</sup> Among all the available anode materials, Li metal is

the ideal anode for SSBs to enable high energy densities of  $>1000 \text{ Wh L}^{-1}$ , due to its highest theoretical specific capacity ( $3860 \text{ mAh g}^{-1}$ ), the lowest negative reduction potential ( $-3.04 \text{ V}$  vs the standard hydrogen electrode) and low density ( $0.59 \text{ g cm}^{-3}$ ).

Extensive research has been conducted on the development of fast  $\text{Li}^+$ -conducting SSEs, including garnet-type conductors,<sup>[4,5,6]</sup> sulfide-based glass/ceramic,<sup>[2]</sup> LISICON-type conductors,<sup>[7]</sup> perovskites,<sup>[8]</sup> etc. Although steady progress has been achieved on  $\text{Li}^+$ -conducting SSEs, most of these SSEs still face challenges including poor thermal/air stability, limited electrochemical window, chemical instability to Li metal, etc. So far, the most critical challenge is how to enhance the capability of suppressing dendrite penetration while maintaining a lower interfacial impedance between SSE and Li metal, particularly under the practical conditions of high current density ( $>1.0 \text{ mA cm}^{-2}$ ).<sup>[9,10–12]</sup> Garnet-type solid electrolytes (GSEs), such as Ta-doped  $\text{Li}_{6.5}\text{La}_3\text{Zr}_{1.5}\text{Ta}_{0.5}\text{O}_{12}$  (LLZTO), are regarded as the ideal SSEs, because of their high  $\text{Li}^+$  ionic conductivity ( $\approx 1 \text{ mS cm}^{-1}$ ), high shear modulus ( $\approx 55 \text{ GPa}$ ), and wide electrochemical stability window.<sup>[4]</sup> To pair the GSEs with lithium anode, quite a few approaches have been used to reduce the interfacial impedance and ensure homogeneous Li dissolution/deposition between GSEs and Li metal, including surface coating (e.g.,  $\text{Al}_2\text{O}_3$ ,<sup>[4,13]</sup>  $\text{Mg}$ ,<sup>[14]</sup> graphite,<sup>[15]</sup> polymers,<sup>[16]</sup>

T. Deng, Dr. H. Jia, Dr. J.-G. Zhang  
Energy and Environmental Directorate  
Pacific Northwest National Laboratory  
902 Battelle Boulevard, Richland, WA 99354, USA  
E-mail: jiguang.zhang@pnnl.gov

T. Deng, Dr. X. Ji, Dr. L. Cao, Dr. P. Wang, Dr. X. Fan,  
Prof. C. Wang  
Department of Chemical and Biomolecular Engineering  
University of Maryland  
College Park, MD 20742, USA  
E-mail: cswang@umd.edu

 The ORCID identification number(s) for the author(s) of this article can be found under <https://doi.org/10.1002/adma.202000030>.

Dr. Y. Zhao, Prof. X. Sun  
Department of Mechanical and Materials Engineering  
University of Western Ontario  
London, Ontario N6A 5B9, Canada

Dr. S. Li, Dr. S. Hwang, Dr. D. Su  
Center for Functional Nanomaterials  
Brookhaven National Laboratory  
Upton, NY 11973, USA

Prof. C. Luo  
Department of Chemistry and Biochemistry  
George Mason University  
Fairfax, VA 22030, USA

Prof. X. Lu  
Department of Applied Engineering Technology  
North Carolina A&T State University  
Greensboro, NC 27411, USA

DOI: 10.1002/adma.202000030

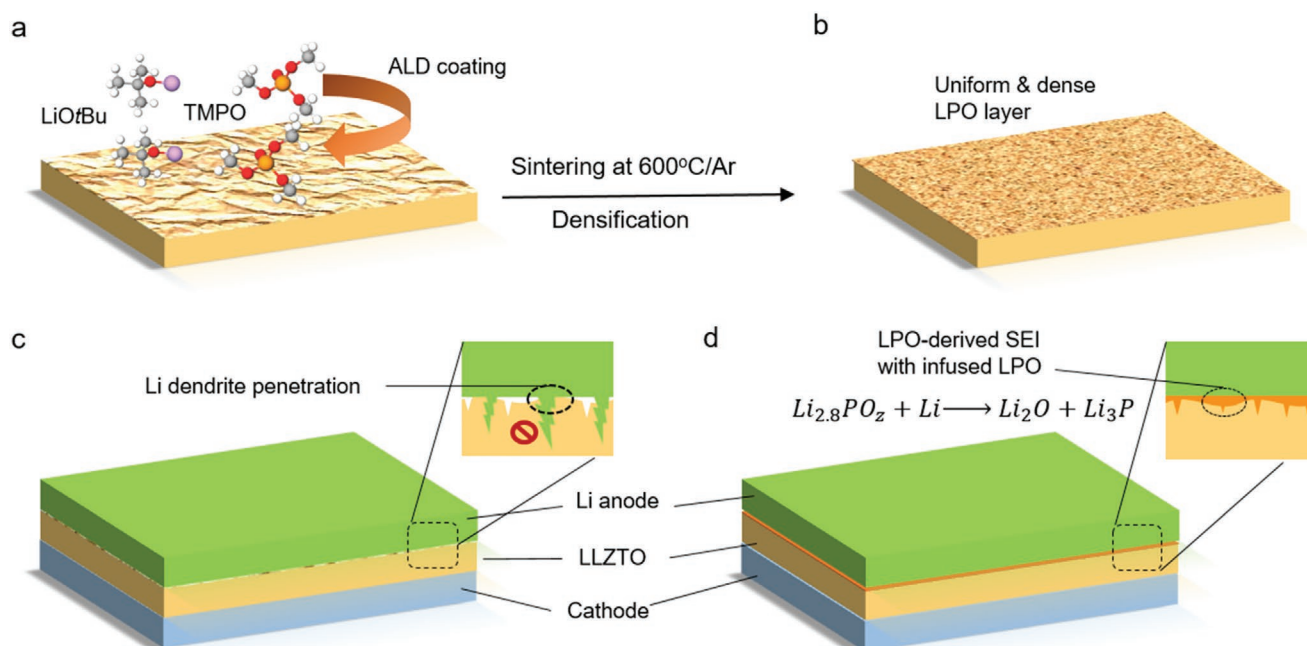


**Figure 1.** Illustration of the interface design of ionic conductive but electronic insulating SEI using atomic layer deposition (ALD). a) Formation of amorphous  $\text{Li}_3\text{PO}_4$  (LPO,  $\approx 10$  nm) layer on polished LLZTO pellet via decomposition of  $\text{LiOtBu}$  and  $\text{TMPO}$ . The pellet presents rough surface with a large amount of cracks and pores due to surface inhomogeneity during sintering. b) Surface densification under high temperature, which helps form uniform and dense LPO interphase (brown). c) Lithium dendrite penetration into the garnet electrolyte, resulting from unstable and weak interface chemistry during cycling with Li anode. d) The top LPO layer stabilizes the Li/LLZTO interface by forming a stable and dense SEI with  $\text{Li}_2\text{O}$ ,  $\text{Li}_3\text{P}$  chemicals (orange). The unreacted dense infused LPO within surface defects or grain boundary acts as a robust shielding to prevent dendrite propagation by improving overall strength of interface.

etc.) and/or heat-treatment<sup>[12,17]</sup> on the SSEs. Nevertheless, most of them can only achieve modest cycling at small current densities ( $<0.4$  mA  $\text{cm}^{-2}$ ) under room temperature (RT), which is far away from the practical current densities (1–10 mA  $\text{cm}^{-2}$ ) for SSBs application. This limitation can be attributed to two factors: 1) the grain boundary chemistry of GSEs cannot prevent or even promote Li dendrite formation at relatively high current density ( $>1.0$  mA  $\text{cm}^{-2}$ ), and 2) solid–solid interfacial impedance continuously increases due to unstable interphase formation and also the loss of contact induced by stress–strain response during cycling.

Recently, moisture has been considered as the main cause of large resistance between GSEs and Li metal anode, because of the  $\text{H}^+/\text{Li}^+$  exchange and formation of  $\text{LiOH}/\text{Li}_2\text{CO}_3$  passivation layer near the surface of pellets.<sup>[10,11,18]</sup> Meanwhile, the intrinsic differences, (e.g., ionic conductivity, shear modulus, electronic conductivity, etc.) between grain boundary structure and the inside grain of SSEs was reported to control the nucleation of Li dendrites at the interface.<sup>[19,20]</sup> To enable a robust Li/GSEs interface for garnet-based solid-state Li metal batteries (SSLBs), it is necessary to take the success of lithium phosphate oxynitride (LIPON) as a reference: The uniform sputtered LIPON film enables high efficiency Li anode via kinetic interface stabilization process, which forms nanometrically thin, Li-ion conductive but electron-insulating interphase.<sup>[21]</sup> On the other hand, the homogenous surface of LIPON film realizes uniform Li dissolution/deposition, which thereby reduces the interface resistance and avoids the formation of localized hot spots for dendrite-like Li nucleation.<sup>[22]</sup>

In this work, we first report to coat the GSEs with a thin layer of solid electrolytes  $\text{Li}_3\text{PO}_4$  (LPO) via atomic layer deposition (ALD) followed by simple annealing process (Figure 1a,b). The as-prepared LPO-infused LLZTO (LPO@LLZTO) presents negligible interfacial resistance ( $\approx 1$   $\Omega\text{cm}^2$ ) to Li anode and excellent stability to moisture. The critical current density (CCD) of LPO@LLZTO reached a record-high value of 2.2 mA  $\text{cm}^{-2}$  at RT, which is five times higher than that of pristine GSEs ( $\approx 0.4$  mA  $\text{cm}^{-2}$ ). The excellent performance of Li/LPO@LLZTO can be attributed to 1) strength-enhanced grain boundary by infused LPO phase, 2) induced homogenous Li dissolution/deposition by LPO layer, as well as 3) formation of stable ionic conductive but electronic insulating P, O-rich solid-electrolyte interphase (SEI) due to LPO reduction (Figure 1c,d). Based on the new chemistry of LPO@LLZTO, a solid cell pairing with  $\text{LiFePO}_4$  cathode is designed and operated using Li metal anode at RT. This study reports a new strategy to create a new type of GSE-based composites for tuning the anode–electrolyte interface chemistry.

As a thin-film deposition technique based on gas phase chemical process, the ALD is able to realize uniform coating on substrate with precisely controlled thickness.<sup>[4,23]</sup> LPO-ALD was chosen here because the LPO solid electrolyte has demonstrated 1) amorphous state with low melting point ( $837$   $^\circ\text{C}$ ) and good mobility at  $600$   $^\circ\text{C}$ ,<sup>[24]</sup> 2) moderate high ionic conductivity ( $\text{Li}_{2.8}\text{PO}_z$ ,  $3.3 \times 10^{-8}$  S  $\text{cm}^{-1}$ ),<sup>[25]</sup> 3) excellent stability to air and moisture, and most importantly, 4) the capability to form an effective SEI once contacting with Li metal.<sup>[26]</sup> What's more, the LPO film has much higher shear modulus (103.4 GPa) than Li

metal (4.2 GPa), which is able to stop Li dendrite penetration based on Monroe and Newman's linear elasticity theory.<sup>[27]</sup>

Ta-doped  $\text{Li}_{6.5}\text{La}_3\text{Zr}_{1.5}\text{Ta}_{0.5}\text{O}_{12}$  pellets utilized in this work are prepared by conventional solid-state method with a high relative density of  $\approx 93\%$ . The detailed preparation procedures are provided in the Supporting Information.<sup>[28]</sup> Ta doping is able to enhance the  $\text{Li}^+$  conductivity and improve the LLZTO stability to Li metal.<sup>[29,30]</sup> Compared with the yellowish pristine LLZTO, the LPO@LLZTO pellet presents light yellow color with glass-shiny sparkle due to the existence of LPO top layer (Figure S1a,b, Supporting Information). The yellowish LLZTO after exposing to air for a long time generates a surface layer of  $\text{Li}_2\text{CO}_3/\text{LiOH}$  mixture, evidenced by the (110), (002) peaks of  $\text{Li}_2\text{CO}_3$  crystal in the X-ray powder diffraction (XRD) pattern (Figure S1c, Supporting Information). Further XRD results in Figure 1a show no difference in the pristine LLZTO and LPO@LLZTO pellet, demonstrating that a high sintering temperature of  $600\text{ }^\circ\text{C}$  did not change the cubic garnet phase of LLZTO. In addition, the ionic conductivity of the LPO@LLZTO pellet at different temperature was measured using Au/LPO@LLZTO/Au blocking cell, which was fabricated by Au sputtering on the surface of disc (Figure S2, Supporting Information). The total conductivity, including bulk and grain boundary parts, is around  $0.5\text{ mS cm}^{-1}$  at RT with an activation energy of  $0.37\text{ eV}$ , which is consistent with the result of pristine LLZTO.<sup>[28,30]</sup>

The Raman spectra of pristine LLZTO (sandpaper-polished), LPO@LLZTO and LLZTO pellets after exposure to ambient moisture for 1 month are shown in Figure 2b. The peaks at  $246$ ,  $375$ ,  $645$ , and  $734\text{ cm}^{-1}$  for pristine LLZTO are characteristics

of the cubic garnet phase while the first two peaks are related to the Li–O bonding in the garnet structure.<sup>[11]</sup> They are not obvious for other two samples due to the covering of thick  $\text{Li}_2\text{CO}_3$  and LPO layers. The strong peak at  $1090\text{ cm}^{-1}$  and weak peak at  $158\text{ cm}^{-1}$ , related to the vibration of  $\text{CO}_3^{2-}$  in ambient moisture-exposed LLZTO, are not detected in the LPO@LLZTO pellet. Meanwhile, the peaks at  $750$ ,  $953$ , and  $1041\text{ cm}^{-1}$  of LPO@LLZTO are the characteristics of  $\text{Li}_3\text{PO}_4$  phase, corresponding to binding vibration of  $\nu_s(\text{O-P-O})$ ,  $\nu_1(\text{PO}_4)$ , and  $\nu_3(\text{PO}_4)$ . The Raman spectra results also indicate that a dense LPO layer on LPO@LLZTO after sintering can prevent  $\text{H}^+/\text{Li}^+$  exchange and formation of  $\text{Li}_2\text{CO}_3$  layer, thus improving the stability of LLZTO pellets to ambient moisture.

Figure 2c,d shows the scanning electron microscopy (SEM) images of the top view of pristine LLZTO after dry-polishing with sandpaper. Compared to the pristine pellet before sandpaper-polishing with uniform La, Ta, Al, Zr, and O elemental distribution (Figure S3, Supporting Information), the polished LLZTO presents a more flat surface, which help keep good contact with Li anode and induce uniform  $\text{Li}^+$  deposition and dissolution. However, the polishing process also exposes a large number of pores and cracks, due to the irregular contraction/expansion during high temperature annealing. Some of these surface defects can even extend to the deep inside of pellet as shown in the inset of Figure 2c, which were reported to promote the lithium nucleation and deposition, thereby leading to dendrite generation.<sup>[6,20,31]</sup> After ALD-coating, the surface defects on LLZTO are covered by the amorphous LPO layer, which also presents uneven surface topography due to irregular

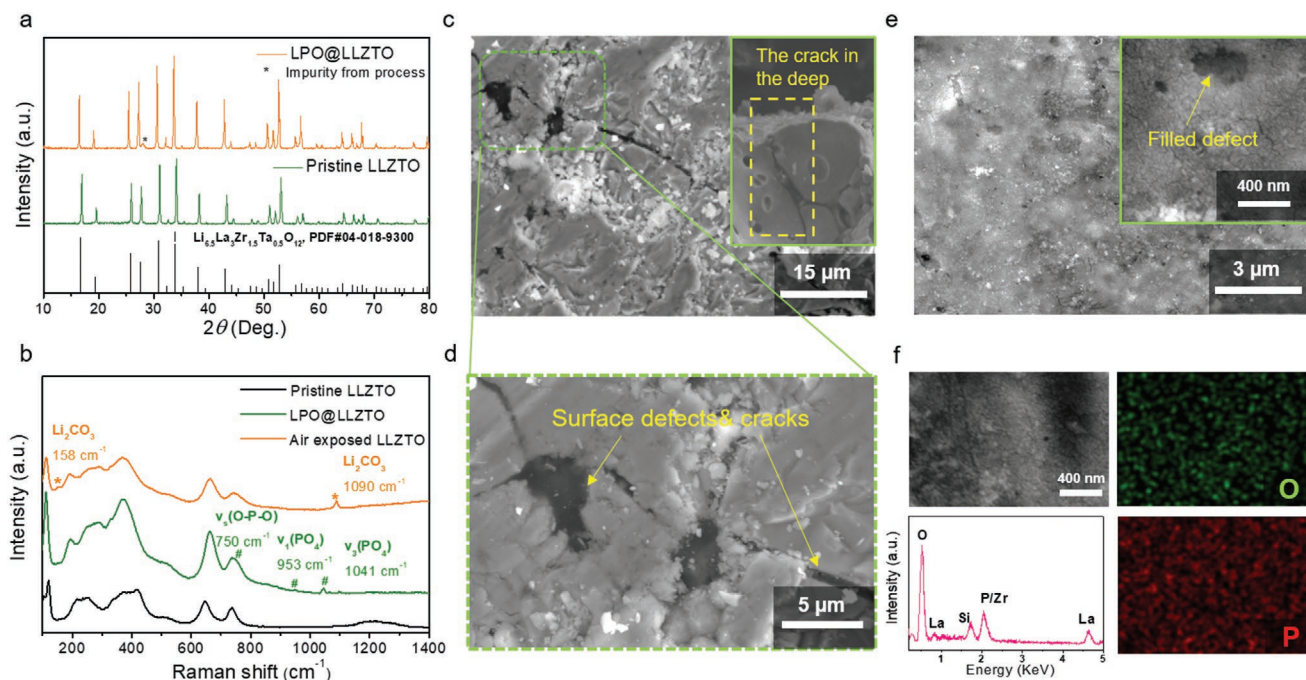


**Figure 2.** Characterization of the LPO@LLZTO garnet electrolyte. a) XRD pattern comparison of the as-prepared pristine LLZTO, LPO@LLZTO, and standard  $\text{Li}_{6.5}\text{La}_3\text{Zr}_{1.5}\text{Ta}_{0.5}\text{O}_{12}$  with pure cubic garnet phase. b) Raman spectra of pristine LLZTO, LPO@LLZTO, and LLZTO after exposure to air for 1 month. c) SEM image for the top view of pristine and polished LLZTO pellet; the inset image shows the crack stretches inside of LLZTO pellet. d) The enlarged view of surface defects and cracks existing on the LLZTO pellet of (c). e) SEM image for the top view of LPO@LLZTO pellet, the inset image showing the enlarged view of filled surface defect by LPO infusion. f) The EDS mapping of O, P elements showing the uniform coating of LPO on LPO@LLZTO.

LPO growth inducing by the defects (Figure S4a,b, Supporting Information). The energy-dispersive X-ray spectroscopy (EDS) on the top surface of coated LLZTO confirms that this ALD layer is rich in O and P elements (Figure S4c,d, Supporting Information). Figure 2e shows the SEM images of dense and uniform top surface of LPO@LLZTO with filled surface defects by LPO layer. Further EDS mapping of LPO@LLZTO confirms that this LPO layer after sintering at 600 °C is rich in O and

P elements (Figure 2f). The unusual signal of Si is from the absorbed crystalline SiO<sub>2</sub>-Al<sub>2</sub>O<sub>3</sub> mixtures during the polishing process using sandpaper.

The impedance plots of the Li symmetric cells based on LPO@LLZTO and pristine LLZTO using electrochemical impedance spectroscopy (EIS) are shown in Figure 3a and Figure S5 in the Supporting Information, respectively. The fitted interfacial area specific resistance (ASR) of the

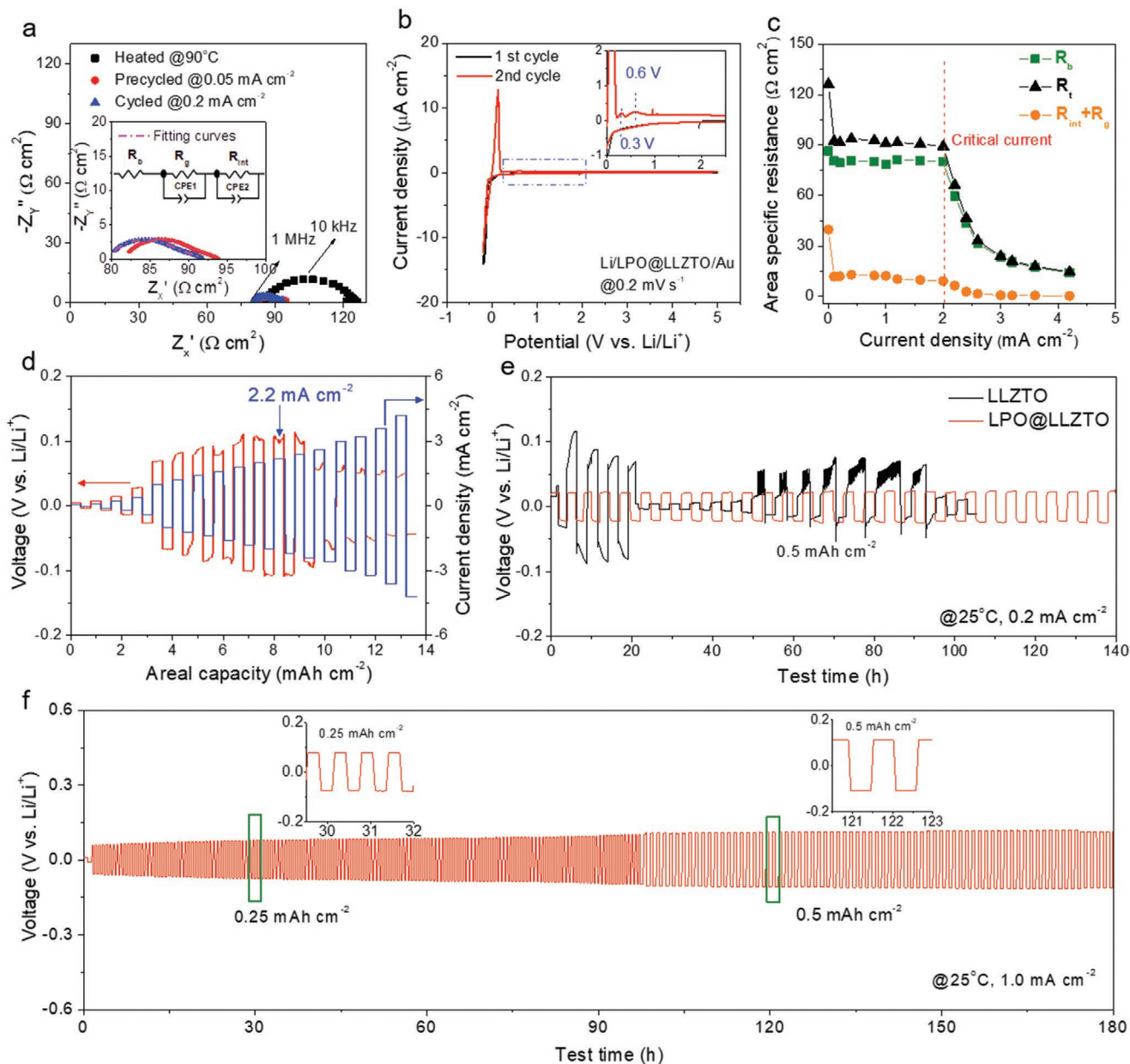


**Figure 3.** Electrochemical characterization of the as-prepared LLZTO pellet at 25 °C. a) Representative EIS spectra of Li/LPO@LLZTO/Li cells before cycling (heat-treated at 90 °C for overnight) and after cycling at 0.05 and 0.2 mA cm<sup>-2</sup>. b) First two cyclic voltammograms of Li/LPO@LLZTO/Au cell at a scanning rate of 0.2 mV s<sup>-1</sup> (-0.2 to 5.0 V). c) Evolution of bulk resistance ( $R_b$ ), total resistance ( $R_t$ ), and interfacial resistance ( $R_{int}$ ) + grain boundary resistance ( $R_g$ ) from EIS spectra of Li/LPO@LLZTO/Li cells after cycling at step-increased current densities. d) Potential responses of Li/LPO@LLZTO/Li cells during the CCD measurement. e) Comparison of d.c. cycling for symmetric cells of Li/LLZTO/Li and Li/LPO@LLZTO/Li at a current density of 0.2 mA cm<sup>-2</sup> under areal capacity of 0.5 mAh cm<sup>-2</sup>. f) Galvanostatic cycling of Li/LPO@LLZTO/Li cell with a current density of 1.0 mA cm<sup>-2</sup>; the cell was precycled at 0.05 mA cm<sup>-2</sup>.

Li/LPO@LLZTO/Li cell is  $17 \Omega \text{ cm}^2$  after heating overnight at  $90^\circ \text{C}$ . It is reduced to  $\approx 1 \Omega \text{ cm}^2$  after precycling at  $0.05 \text{ mA cm}^{-2}$  and maintains this value under high current density of  $0.2 \text{ mA cm}^{-2}$ . A detailed calculation and comparison for interfacial ASR are compiled in Table S1 in the Supporting Information. The ultrasmall interfacial ASR is almost five times lower than that of pristine LLZTO, which can be attributed to: 1) the flat surface of LPO@LLZTO created by LPO infiltration and 2) formation of new  $\text{Li}^+$  conductive interphase in precycling. The formation of new interphase can be confirmed by the peaks at 0.3 and 0.6 V for anodic scan in the cyclic voltammetry (CV) curves using Li/LPO@LLZTO/Au cell (Figure 3b). The redox peaks indicate this new interphase is relative stable and might help prevent the LLZTO from reduction in cycling.

To demonstrate the capability to suppress Li dendrite, CCD of LPO@LLZTO using Li symmetric cells was investigated under a fixed areal capacity condition ( $0.4 \text{ mAh cm}^{-2}$ ) at RT. Figure 3c shows the evolution of bulk resistance ( $R_b$ ), total resistance ( $R_t$ ), and interfacial resistance ( $R_{\text{int}}$ ) + grain boundary resistance ( $R_g$ ) of a Li/LPO@LLZTO/Li cell during the CCD measurement. The detailed EIS plots have been provided in Figure S6 in the Supporting Information, where the length of depressed semicircle shows the magnitude of ( $R_{\text{int}} + R_g$ ), while the interception on  $x$ -axis is the magnitude of  $R_b$ . As shown in Figure 3c, when current density gradually increases from 0.1 to  $2.0 \text{ mA cm}^{-2}$ , both the ( $R_{\text{int}} + R_g$ ) and  $R_b$  keep almost constant ( $12 \Omega \text{ cm}^2$  vs  $80 \Omega \text{ cm}^2$ ), which indicates the excellent toleration of high current density for LPO@LLZTO pellet. Further cycling at  $>2.2 \text{ mA cm}^{-2}$ , both the ( $R_{\text{int}} + R_g$ ) and  $R_b$  experience a continual decrease to 0.4 and  $13 \Omega \text{ cm}^2$  at  $4.2 \text{ mA cm}^{-2}$ , indicating reduction of  $\text{Li}^+$  transfer distance and enhancement of contacting between Li metal and LLZTO due to Li dendrite growth.

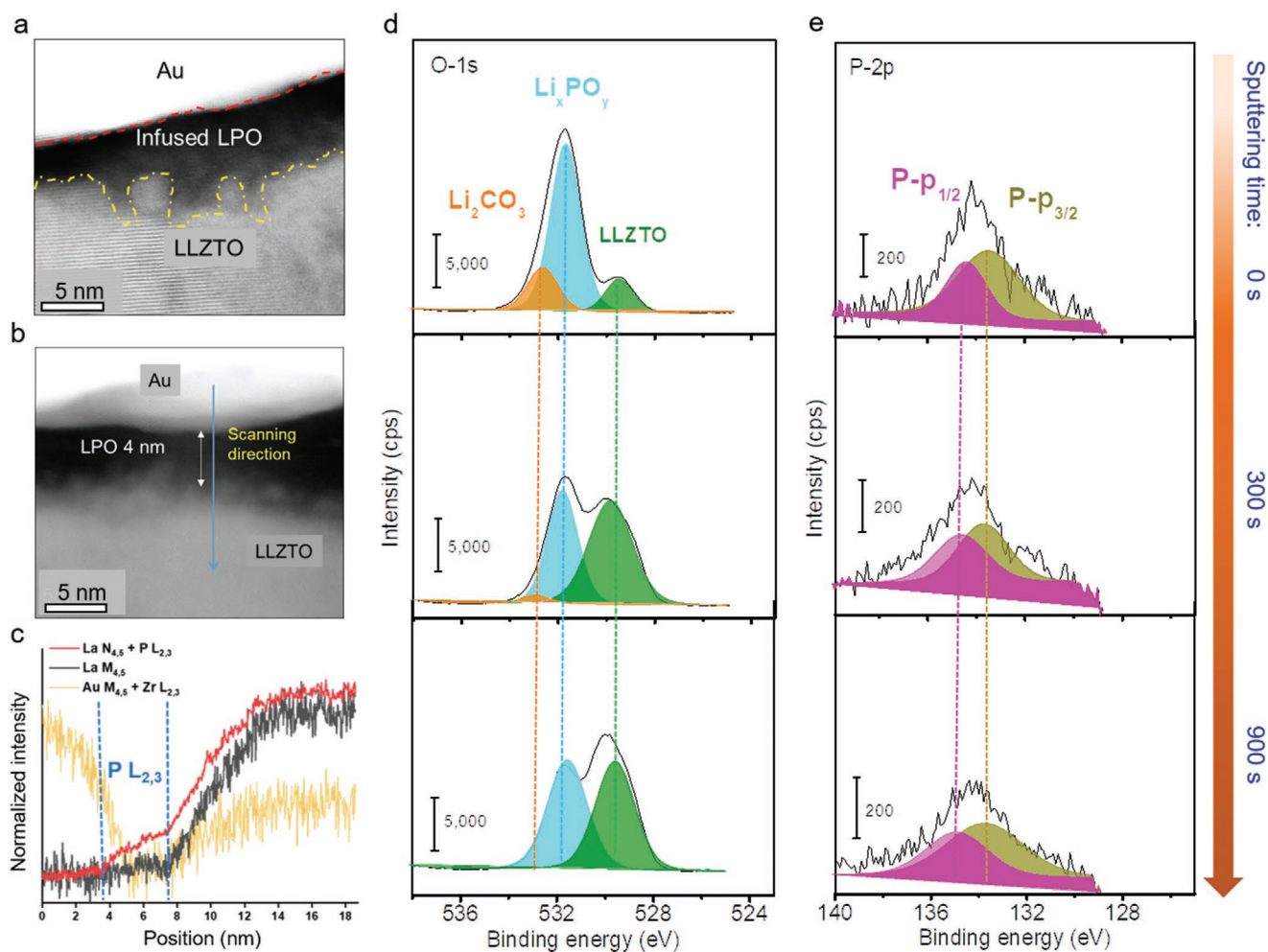
The corresponding potential response in Figure 3d shows small and flat voltage profiles ( $<80 \text{ mV}$ ) when current densities are below  $1.2 \text{ mA cm}^{-2}$ . But at high current densities, such as  $1.4 \text{ mA cm}^{-2}$  and above, the cell voltage presents a slope with some fluctuations. Once the current density reaches a critical value of  $2.2 \text{ mA cm}^{-2}$ , the cell experiences an apparent voltage drop from 110 mV, indicating Li dendrite penetration across the electrolyte and a partial short circuit occurred. The voltage fluctuation at high current densities ( $>1.2 \text{ mA cm}^{-2}$ ) is due to the pore generation and change of surface contact by large amount of Li deposition/dissolution.<sup>[32]</sup> As a comparison, the CCD of pristine LLZTO is around  $0.4 \text{ mA cm}^{-2}$  with a high voltage of 70 mV for Li/LLZTO/Li cell under a fixed areal capacity of  $0.2 \text{ mAh cm}^{-2}$  (Figure S7a, Supporting Information). The corresponding impedance spectrum at the current density of  $0.4 \text{ mA cm}^{-2}$  shows a small semicircle (see the inset in Figure S7b in the Supporting Information), confirming the short-circuit of Li symmetric cell.

Figure 3e shows a comparison of d.c. cycling for Li symmetric cells of Li/LLZTO/Li Li/LPO@LLZTO/Li at a current density of  $0.2 \text{ mA cm}^{-2}$  under fixed areal capacity of  $0.5 \text{ mAh cm}^{-2}$ . The Li symmetric cell with LPO@LLZTO presents a small voltage of 20 mV and can be stabilized for more than 140 h at RT. When cycled under  $0.6 \text{ mA cm}^{-2}$  and fixed areal capacity of  $0.15 \text{ mAh cm}^{-2}$ , the cell is able to maintain for more than 800 h while keeping a small voltage of  $\approx 65 \text{ mV}$  (Figure S8, Supporting Information), indicating the highly stable Li/LPO@

LLZTO interface. On contrary, the cell with pristine LLZTO presents small voltage of 16 mV first but continually increases in the following cycles (Figure 3e). The large polarization finally causes the short of cell after 20 h by presenting an extreme small voltage of  $\approx 4 \text{ mV}$ . The melting of Li dendrite by joule heat due to high local current density at some spots leads some fluctuation of voltage although the Li symmetric cell has been shorted. We then characterized the cycled Li/LLZTO interface recovered from the shorted Li/LLZTO/Li cell via SEM (Figure S9, Supporting Information). Apparently, some parts of the Li metal anode have been detached from the LLZTO pellet due to Li volume change induced by a large amount of Li dissolution/deposition, which well explains the sharp increment of cell polarization in Figure 3e. More importantly, we find the distribution of surface cracks on top surface of LLZTO highly matches with the black shorted area on LLZTO pellet (Figure S10a–c, Supporting Information). The Li can also deposit into the LLZTO pellet via the surface defects or cracks after Li penetration occurs due to increase of electronic conductivity (Figure S10d, Supporting Information), which is consistent with previous works.<sup>[31]</sup>

For comparison, we further cycled the Li/LPO@LLZTO/Li cell with a current density of  $1.0 \text{ mA cm}^{-2}$  under areal capacities of 0.25 and  $0.5 \text{ mAh cm}^{-2}$ . As shown in Figure 3f, the cell voltage always keeps  $<100 \text{ mV}$  for  $0.25 \text{ mAh cm}^{-2}$  and  $\approx 110 \text{ mV}$  for  $0.5 \text{ mAh cm}^{-2}$  during a long cycling time of 180 h. The small increase of voltage might be related to the pore creation on Li anode side, which reduces the contact area between LPO@LLZTO and Li anode. Actually, operating the symmetric Li cells at high temperature and pressure have been proved an effective way to achieve good Li/SSEs interface and reduce the polarization.<sup>[6,12,32]</sup> It needs to be emphasized that the most recent reported symmetric Li cells with coated GSEs can be only cycled at small current densities ( $<0.3 \text{ mA cm}^{-2}$ ) with small areal capacities ( $\approx 0.1 \text{ mAh cm}^2$ ) at RT (Table S2, Supporting Information). For our work, the excellent electrochemical performance of LPO@LLZTO at RT and normal pressure conditions makes a big step forward to practical SSLBs at ambient conditions.

To understand the excellent performance of LPO@LLZTO, it is necessary to know the LPO distribution across the surface of LLZTO pellet. As shown in the high-angle annular dark-field scanning transmission electron microscopy (HAADF-STEM) of surface sample prepared by focused ion beam (FIB) cut from the LPO@LLZTO, the LPO layer shows highly affinity to LLZTO pellet with a trend of internal expansion or diffusion into grain boundary (Figure 4a). Figure S11 in the Supporting Information shows the surface porosity and grain boundary structure below the surface of LLZTO during FIB sampling, which have been regarded as the channel for the Li dendrite penetration. These results confirm that the uniform-distributed ALD-LPO coating layer on the surface of garnet LLZTO pellet. Further electron energy loss spectroscopy (EELS) line scan analysis along the LPO/LLZTO indicates the thickness of LPO layer after sintering is different ( $<5 \text{ nm}$ ) due to the infusion of LPO (Figure 4b,c; Figure S12, Supporting Information). Considering the overlapping of P-L<sub>2,3</sub> edge and La-M<sub>4,5</sub> signals in EESL mode, the P distribution for determining the thickness of LPO layer can be observed by comparing the evolution of La-M<sub>4,5</sub> edge along the LPO/LLZTO interface.



**Figure 4.** Characterization for the top LPO layer and infused LPO in grain boundary of LLZTO pellet. a) Typical dark-filed cross-section TEM image at the interface of LPO@LLZTO with the Au coating layer. b) TEM-HAADF image of LPO@LLZTO interface for EELS line scan analysis; the thickness of the infused LPO layer is <5 nm after sintering. c) Compositional line scan profiles for La-M<sub>4,5</sub> + P-L<sub>2,3</sub> edge, La-M<sub>4,5</sub> edge, and Au-M<sub>4,5</sub> + Zr-L<sub>2,3</sub> edge along the scanned line probed in EELS mode; the P distribution can be observed by comparing the evolution of La-M<sub>4,5</sub> edge due to overlapping of P-L<sub>2,3</sub> edge and La-M<sub>4,5</sub> signals. d,e) XPS depth profiles of O 1s (d) and P 2p (e); the XPS signal after long time of Ar<sup>+</sup> sputtering indicates the presence of LPO inside LLZTO pellet. CPS: counts per second.

Figure 4d,e shows the X-ray photoelectron spectroscopy (XPS) depth profiles of O 1s and P 2p from as-prepared LPO@LLZTO with Ar<sup>+</sup> sputtering times of 0, 300, and 900 s. For LPO@LLZTO, the O signal is mainly from surface Li<sub>2</sub>CO<sub>3</sub> (532.5 eV), Li<sub>x</sub>PO<sub>y</sub> (531.8 eV), and LLZTO (529.4 eV), while the P signal (133.2 eV for P-p<sub>3/2</sub>, 134.4 eV for P-p<sub>1/2</sub>) confirms the existence of LPO phase on the surface or subsurface of LLZTO pellet. As the sputtering time increase from 0 to 900 s, the peak for Li<sub>2</sub>CO<sub>3</sub> gets weaker and finally disappears, while the peak for LLZTO becomes stronger. Meanwhile, the signals for P 2p and Li<sub>x</sub>PO<sub>y</sub> always keep constant during Ar<sup>+</sup> sputtering, indicating the thickness of LPO phase is >15 nm due to the infusion of LPO phase, considering a sputtering of 900 s etches about 15 nm of LLZTO in thickness. The tiny amount of Li<sub>2</sub>CO<sub>3</sub> on LPO@LLZTO might originate from the decomposition of organic components of precursors during ALD process.

The dense and uniform LPO layer on LPO@LLZTO (Figure 2e) also helps prevent the happening of H<sup>+</sup>/Li<sup>+</sup> exchange and formation of Li<sub>2</sub>CO<sub>3</sub> in air moisture, which is

essential in the fabrication of SSBs. To demonstrate the moisture stability of LPO@LLZTO, the XPS depth profiles of C 1s for LLZTO and LPO@LLZTO pellets after exposing to ambient air for one month have been provided in Figure S13 in the Supporting Information with different Ar<sup>+</sup> sputtering time. The two peaks at 285.8 and 290.7 eV in the C 1s spectrum of the LLZTO pellet correspond to carbon and carbonate species, which might be from the sandpaper-polishing process and reaction with H<sub>2</sub>O and CO<sub>2</sub> in ambient air. Ratio of Li<sub>2</sub>CO<sub>3</sub> to the C peak of the air-exposed LLZTO increases from 0.85 to 1.62 and 2.07 after sputtering for 300 and 900 s, which indicates that a thick layer of Li<sub>2</sub>CO<sub>3</sub>-passivation layer is formed on LLZTO. These results are further confirmed by the XPS depth profiles for O 1s and Li 1s (Figure S14, Supporting Information). But for LPO@LLZTO, the XPS depth profiles of C 1s only present a tiny amount of Li<sub>2</sub>CO<sub>3</sub> component, which keeps consistent with the O 1s depth profiles in Figure 4d. After sputtering for 300 and 900 s, the peaks for Li<sub>2</sub>CO<sub>3</sub> in C 1s spectra almost disappear, which confirms the excellent protection of air-stable LPO

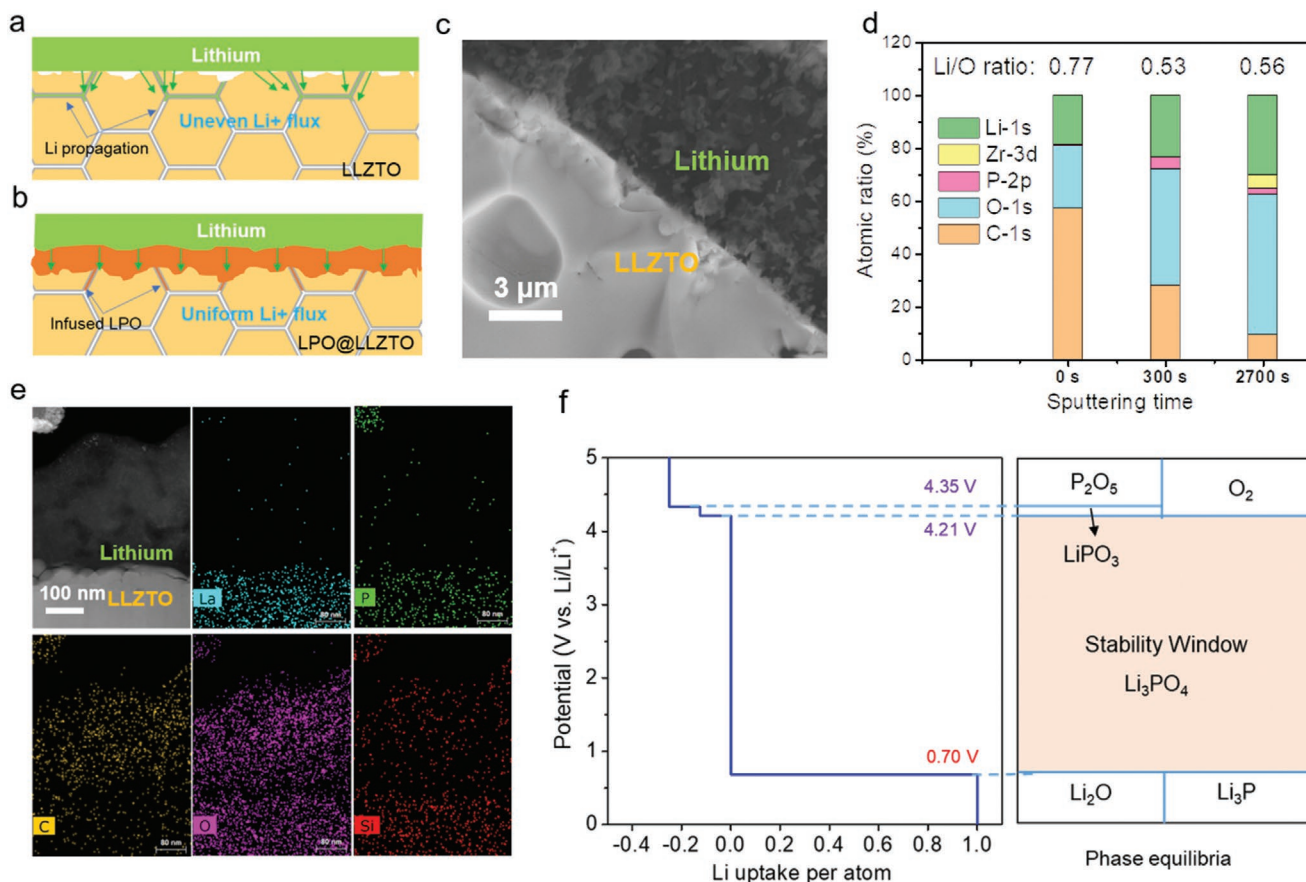


**Figure 5.** Illustration of interface chemistry for robust and Li-ion conductive Li/LPO@LLZTO interface. a) Schematics of lithium dendrite propagation and b) proposed mechanisms at the interface of Li/LLZTO. c) SEM image of Li/LPO@LLZTO interface cycled at  $1.0 \text{ mA cm}^{-2}$  with an areal capacity of  $0.5 \text{ mAh cm}^{-2}$ . d) Composition of cycled Li/LPO@LLZTO interface after various durations of  $\text{Ar}^+$  sputtering. e) STEM-EDS mappings of La, P, C, O, and Si elements on FIB-cut cycled Li/LPO@LLZTO interface. f) First-principles calculation results of the voltage profile and phase equilibria of LPO solid electrolyte upon lithiation and delithiation.

layer from the parasitic reactions between LLZTO and ambient moisture.

Compared to pristine LLZTO, the LPO@LLZTO is able to regulate the  $\text{Li}^+$  flux and realize smooth Li deposition/dissolution via LPO phase (Figure 5a,b), thus keeps good contact with Li anode even after cycling at  $1.0 \text{ mA cm}^{-2}$  (Figure 5c). To demonstrate the proposed mechanism, the interfacial composition of Li/LPO@LLZTO and Li/LLZTO interfaces harvested from Li symmetric cell after cycling at  $0.2 \text{ mA cm}^{-2}$  was examined using high-resolution XPS. As shown in Figure S15 in the Supporting Information, the O 1s spectra with sputtering time of 300 and 2700 s for LPO@LLZTO consists the peaks of  $\text{Li}_2\text{CO}_3$  (532.5 eV),  $\text{Li}_x\text{PO}_y$  (531.8 eV), LLZTO (529.6 eV), and  $\text{Li}_2\text{O}$  (528.8 eV), while the P 2p signal demonstrates the formation of P compounds for LPO@LLZTO pellet. Indicated by the peaks of O 1s and P 2p depth profiles, the SEI component is exposed after sputtering for 300 s. However, since thickness of LPO-derived SEI is relatively small, it is hard to distinguish the detailed information of P-derived components within the SEI.

Figure 5d and Figure S16a in the Supporting Information compare the SEI elemental compositions of LPO@LLZTO and LLZTO with different sputtering depth. Different from the pristine LLZTO with a constant high Li/O ratio of  $\approx 0.9$ , the SEI

of LPO@LLZTO present much lower Li/O ratio of  $\approx 0.5$ . The table in Figure S16b in the Supporting Information compares the atomic ratios for some possible components within SEI, including  $\text{Li}_2\text{CO}_3$ ,  $\text{Li}_3\text{PO}_4$ , LLZTO,  $\text{Li}_2\text{O}$ , and  $\text{Li}_3\text{P}$ , confirming that the main SEI components of LPO@LLZTO are LPO-derived components with less O. After sputtering for 2700 s, the LPO@LLZTO of O 1s spectra exposes a significant high signal of LLZTO (Figure S15a, Supporting Information), while it still presents high content of  $\text{Li}_2\text{O}$  for the pristine LLZTO (Figure S17a–c, Supporting Information). The Ta 4f spectra in Figure S17d–f in the Supporting Information shows pretty good crystal of Ta compounds with 5+ valence for the SEI of Li/LLZTO interface, which is due to relative high stability of Ta dopants to Li metal.<sup>[30,33]</sup> However, compared with the LPO@LLZTO, the two peaks of  $3d_{3/2}$  (184.2 eV) and  $3d_{5/2}$  (181.8 eV) for  $\text{Zr}^{4+}$  in pristine LLZTO after cycling are undistinguishable, indicating the  $\text{Zr}^{4+}$  reduction by Li metal (Figure S18, Supporting Information).<sup>[34]</sup> These results confirm that the formation of thick  $\text{Li}_2\text{O}$ -rich SEI for Li/LLZTO interface due to the LLZTO reduction during long cycling.

The STEM-EDS mappings of FIB-cut cycled Li/LPO@LLZTO interface shows the uniform distribution of P beneath the surface of LPO@LLZTO due to infusion of LPO phase (Figure 5e).

The additional C and O signals on Li metal might be from the sample preparation because of the exposing to air, while the existence of Si is consistent with the EDS compositional analysis of LPO in Figure 2. On a large scale, the SEM-EDS mappings of O and P elements for Li/LPO@LLZTO interface shows a relative high signal of P element in some specific pots, which might be due to the LPO-filled surface defects (Figure S19, Supporting Information). To find the compositional difference across the Li/LPO@LLZTO interface, the EELS-line scan have been conducted to get the profiles of La-M<sub>4,5</sub> edge, P K-edge, O-K edge, and Au-M<sub>4,5</sub> edge along the yellow line in TEM-HAADF image of interface (Figure S20, Supporting Information). Compared with the rich P element inside of LPO@LZT, the relative weaker signal of P element near the Li metal indicates the formation of new SEI phase by LPO reduction, which has also been observed in CV curves of Li symmetric cell (Figure 3b). What's more, the DC polarization curves of Au/LLZTO/Au and Au/LPO@LLZTO/Au cells shows the LPO modification lowers the electronic conductivity of LLZTO from 10<sup>-8</sup> to ≈10<sup>-9</sup> S cm<sup>-1</sup> at RT (Figure S21, Supporting Information).

To further reveal the reaction mechanism near the Li/LPO@LLZTO interface, the Li grand potential phase diagram from the

first-principles calculation is provided to identify the thermal phase equilibria at different potentials for LPO (Figure 5f). We chose the pure Li<sub>3</sub>PO<sub>4</sub> crystal phase for the calculation, considering the complex phase information of ALD-LPO. The calculated voltage profile and phase equilibria of LPO upon lithiation and delithiation confirm the LPO is thermodynamically unstable to Li metal. The reduction of the LPO starts at 0.7 V, where LPO is lithiated and turns into Li<sub>2</sub>O and Li<sub>3</sub>P. This value is also very close to additional redox peak (0.6 V) at CV curve (Figure 3b). At much higher potential of 4.21 and 4.35 V, the LPO tends to be oxidized to form P<sub>2</sub>O<sub>5</sub> with the releasing of O<sub>2</sub>, which means the LPO is also helpful to enhance the oxidation ability of LLZTO. In summary, our calculation and experimental results have shown that the LPO layer on LPO@LLZTO is able to form a stable LPO-derived SEI by preventing the continual reduction of LLZTO, while the infused LPO improves the overall stability and Li<sup>+</sup> conductivity of LLZTO.

The stable interface between GSEs and Li metal anode enabled by our new type of LPO@LLZTO composite is the key to enable all kinds of high-energy-density Li metal batteries. By coupling with a LiFePO<sub>4</sub> composite cathode, a solid-state Li/LPO@LLZTO/LiFePO<sub>4</sub> battery was fabricated to demonstrate

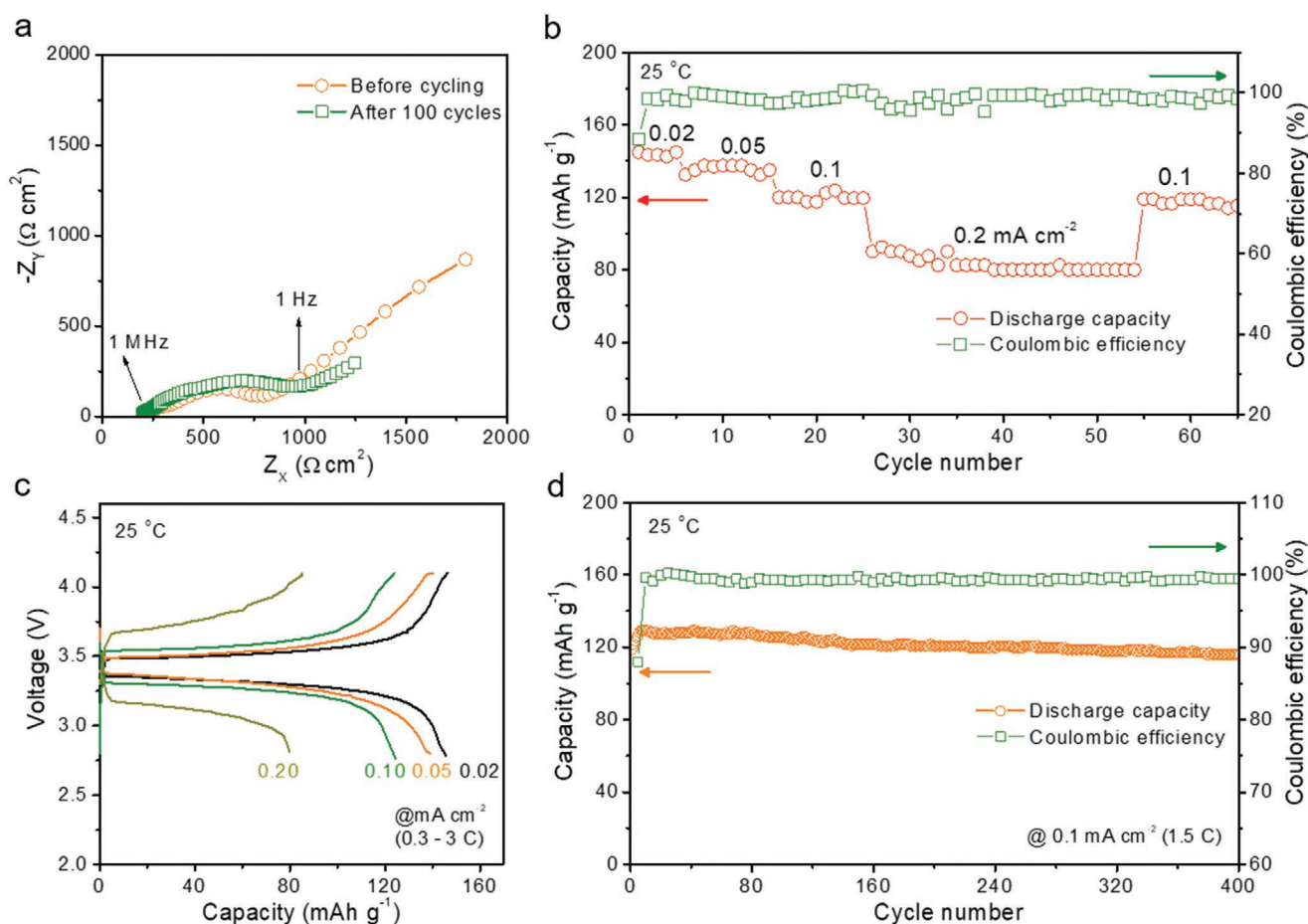


**Figure 6.** Demonstration of solid-state batteries by pairing with LiFePO<sub>4</sub> cathode. a) Nyquist spectra of solid cell before and after 100 cycles with constant current density of 0.1 mA cm<sup>-2</sup>. b) Rate capability of Li/LPO@LLZTO/LiFePO<sub>4</sub> solid cell at different current densities, increasing from 0.02 to 0.20 mA cm<sup>-2</sup> (0.3C–3C, 1C = 140 mA g<sup>-1</sup>). c) Corresponding electrochemical charge/discharge curves of solid cell at different current densities. d) Cycling performance of Li/LPO@LLZTO/LiFePO<sub>4</sub> solid cell at 0.1 mA cm<sup>-2</sup> (1.5C). The areal capacity of LiFePO<sub>4</sub> composite cathode is ≈1.0 mg cm<sup>-2</sup>.

the feasibility of LPO@LLZTO for SSLBs. To enhance the Li transfer kinetics within the cathode film, the composite cathode was applied via conventional slurry coating on Al foil by consisting of LiFePO<sub>4</sub> powder, polyvinylidene fluoride (PVDF), LiTFSI, LLZTO powder, and carbon black with a weight ratio of 50:25:10:10:5.<sup>[35]</sup> During the cell assembling, some tiny amount of ethylene carbonate (EC) solvent was added as plasticizer to the LiFePO<sub>4</sub> composite cathode for enhancing the contact between LPO@LLZTO pellet and electrode.

The resistances of LiFePO<sub>4</sub> full cell based on the Li/LPO@LLZTO were investigated via EIS. As shown in Figure 6a, only one depressed semicircle can be observed, where the high-frequency and low-frequency portions of the semicircles are assigned to grain boundary and interfacial resistances between LPO@LLZTO and electrode, respectively.<sup>[4,11,36]</sup> The high-frequency intersection of the semicircles with the real axis is the bulk resistance of LPO@LLZTO pellet. Thus, the total EIS ASR of the Li/LPO@LLZTO/LiFePO<sub>4</sub> cells is around 850 and 1000 Ω cm<sup>2</sup> before cycling and after 100 cycles at RT. The large bulk resistance (230 Ω cm<sup>2</sup>) and interfacial resistance plus grain boundary resistance (620 Ω cm<sup>2</sup>) indicates there are still some room to improve the cell performance by lowering the resistances between cathode and LPO@LLZTO, as well as within the LiFePO<sub>4</sub> composite cathode.

Figure 6b shows the rate capability of the battery when charged/discharged with the current densities ranging from 0.02 to 0.2 mA cm<sup>-2</sup>. As can be seen, the battery can deliver high capacities of 143, 137, 122, and 84 mAh g<sup>-1</sup> at current densities of 0.02, 0.05, 0.1, and 0.2 mA cm<sup>-2</sup>, respectively, while showing an high average Coulombic efficiency of >99%. The corresponding electrochemical charging/discharging curves in Figure 6c validate the good rate performance of the cell under different current densities between 2.8 and 4.1 V. The cell also shows good long-term stability at 0.1 mA cm<sup>-2</sup> (1.5C) with high retention of 88% over 400 cycles and a high Coulombic efficiency of >99% (Figure 6d), demonstrating the feasibility of full cells based on the highly stable Li/LPO@LLZTO interface.

In summary, we proposed a new type of LPO@LLZTO composites that addressed the most challenging interfacial issue between Li metal anode and garnet-type LLZTO solid electrolyte for SSLBs. The LLZTO pellet with ultrathin LPO-ALD coating after sintering presents continual infused LPO phase inside while keeping an air-stable and uniform LPO layer on the pellet, which protects the GSEs from H<sup>+</sup>/Li<sup>+</sup> exchange/passivation film formation. As a result, the LPO@LLZTO shows negligible interfacial resistance ASR (≈1 Ω cm<sup>2</sup>) to Li anode and stable cycling for >180 h in symmetric lithium cell configuration even under large current density of 1.0 mA cm<sup>-2</sup>. The CCD of LPO@LLZTO reaches a record-high value of 2.2 mA cm<sup>-2</sup> at RT, which met the practical requirement of solid-state batteries. A solid-state Li metal cell based on the interface engineering on Li/LPO@LLZTO achieves excellent rate performance and cycling stability. The remarkably enhanced performances of LPO@LLZTO can be ascribed to three aspects: 1) flat LPO top layer enables conformal contact with Li anode, leading to uniform Li stripping/plating; 2) infused LPO fills the surface defects while improves the mechanical strength and Li-ion conductivity of interconnected grain boundary structures; and 3) the formation of Li<sub>2</sub>O, Li<sub>3</sub>P-rich SEI with negligible electronic

conduction and high Li-ion conduction. The present work resolves the most challenging interfacial issues for garnet SSEs and Li metal anode, and is thus a major breakthrough toward the development of high-energy-density and safe SSLBs.

## Supporting Information

Supporting Information is available from the Wiley Online Library or from the author.

## Acknowledgements

This work was supported by the Assistant Secretary for Energy Efficiency and Renewable Energy, Office of Vehicle Technologies of the US Department of Energy (DOE) through the Advanced Battery Materials Research (BMR) program under contract no. DE-AC02-05CH11231. T.D. is grateful for financial support from the Engie Chuck Edwards Memorial Fellowship at the University of Maryland. The authors gratefully acknowledge the support of the Maryland NanoCenter and its AIM Lab. The work done at Brookhaven National Laboratory was supported by the Assistant Secretary for Energy Efficiency and Renewable Energy, Vehicle Technology Office of the U.S. Department of Energy through the Advanced Battery Materials Research (BMR) Program, including Battery500 Consortium under contract DE-SC0012704. The authors also thank Y. Wang from PNNL for the preparation of LLZTO.

## Conflict of Interest

The authors declare no conflict of interest.

## Keywords

garnet electrolytes, interfacial chemistry, lithium dendrites, solid-electrolyte interphase, solid-state batteries

Received: January 2, 2020

Revised: March 25, 2020

Published online:

- [1] a) D. Lin, Y. Liu, Y. Cui, *Nat. Nanotechnol.* **2017**, *12*, 194; b) J. W. Choi, D. Aurbach, *Nat. Rev. Mater.* **2016**, *1*, 16013; c) G. Ceder, Y. M. Chiang, D. R. Sadoway, M. K. Aydinol, Y. I. Jang, B. Huang, *Nature* **1998**, *392*, 694.
- [2] Y. Kato, S. Hori, T. Saito, K. Suzuki, M. Hirayama, A. Mitsui, M. Yonemura, H. Iba, R. Kanno, *Nat. Energy* **2016**, *1*, 16030.
- [3] N. Kamaya, K. Homma, Y. Yamakawa, M. Hirayama, R. Kanno, M. Yonemura, T. Kamiyama, Y. Kato, S. Hama, K. Kawamoto, A. Mitsui, *Nat. Mater.* **2011**, *10*, 682.
- [4] X. Han, Y. Gong, K. K. Fu, X. He, G. T. Hitz, J. Dai, A. Pearse, B. Liu, H. Wang, G. Rubloff, Y. Mo, V. Thangadurai, E. D. Wachsman, L. Hu, *Nat. Mater.* **2017**, *16*, 572.
- [5] a) Q. Liu, Z. Geng, C. Han, Y. Fu, S. Li, Y.-b. He, F. Kang, B. Li, *J. Power Sources* **2018**, *389*, 120; b) R. Murugan, V. Thangadurai, W. Weppner, *Angew. Chem., Int. Ed.* **2007**, *46*, 7778.
- [6] A. Sharafi, H. M. Meyer, J. Nanda, J. Wolfenstine, J. Sakamoto, *J. Power Sources* **2016**, *302*, 135.
- [7] a) P. Knauth, *Solid State Ionics* **2009**, *180*, 911; b) G. F. Ortiz, M. C. López, P. Lavela, C. Vidal-Abarca, J. L. Tirado, *Solid State Ionics* **2014**, *262*, 573.

- [8] N. Bonanos, K. Knight, B. Ellis, *Solid State Ionics* **1995**, 79, 161.
- [9] a) C. L. Tsai, V. Roddatis, C. V. Chandran, Q. Ma, S. Uhlenbruck, M. Bram, P. Heitjans, O. Guillon, *ACS Appl. Mater. Interfaces* **2016**, 8, 10617; b) F. Han, A. S. Westover, J. Yue, X. Fan, F. Wang, M. Chi, D. N. Leonard, N. J. Dudney, H. Wang, C. Wang, *Nat. Energy* **2019**, 4, 187.
- [10] A. Sharafi, E. Kazyak, A. L. Davis, S. Yu, T. Thompson, D. J. Siegel, N. P. Dasgupta, J. Sakamoto, *Chem. Mater.* **2017**, 29, 7961.
- [11] Y. Li, X. Chen, A. Dolocan, Z. Cui, S. Xin, L. Xue, H. Xu, K. Park, J. B. Goodenough, *J. Am. Chem. Soc.* **2018**, 140, 6448.
- [12] N. J. Taylor, S. Stangeland-Molo, C. G. Haslam, A. Sharafi, T. Thompson, M. Wang, R. Garcia-Mendez, J. Sakamoto, *J. Power Sources* **2018**, 396, 314.
- [13] Y. Liu, Q. Sun, Y. Zhao, B. Wang, P. Kaghazchi, K. R. Adair, R. Li, C. Zhang, J. Liu, L. Y. Kuo, Y. Hu, T. K. Sham, L. Zhang, R. Yang, S. Lu, X. Song, X. Sun, *ACS Appl. Mater. Interfaces* **2018**, 10, 31240.
- [14] K. K. Fu, Y. Gong, Z. Fu, H. Xie, Y. Yao, B. Liu, M. Carter, E. Wachsman, L. Hu, *Angew. Chem., Int. Ed.* **2017**, 56, 14942.
- [15] Y. Shao, H. Wang, Z. Gong, D. Wang, B. Zheng, J. Zhu, Y. Lu, Y.-S. Hu, X. Guo, H. Li, X. Huang, Y. Yang, C.-W. Nan, L. Chen, *ACS Energy Lett.* **2018**, 3, 1212.
- [16] W. Zhou, S. Wang, Y. Li, S. Xin, A. Manthiram, J. B. Goodenough, *J. Am. Chem. Soc.* **2016**, 138, 9385.
- [17] M. Wang, J. B. Wolfenstine, J. Sakamoto, *Electrochim. Acta* **2019**, 296, 842.
- [18] a) M. Nyman, T. M. Alam, S. K. McIntyre, G. C. Bleier, D. Ingersoll, *Chem. Mater.* **2010**, 22, 5401; b) A. Sharafi, S. Yu, M. Naguib, M. Lee, C. Ma, H. M. Meyer, J. Nanda, M. Chi, D. J. Siegel, J. Sakamoto, *J. Mater. Chem. A* **2017**, 5, 13475.
- [19] J. Wolfenstine, J. L. Allen, J. Sakamoto, D. J. Siegel, H. Choe, *Ionics* **2018**, 24, 1271.
- [20] T. Krauskopf, R. Dippel, H. Hartmann, K. Peppler, B. Mogwitz, F. H. Richter, W. G. Zeier, J. Janek, *Joule* **2019**, 3, 2030.
- [21] a) A. Schwöbel, R. Hausbrand, W. Jaegermann, *Solid State Ionics* **2015**, 273, 51; b) T. Famprakis, P. Canepa, J. A. Dawson, M. S. Islam, C. Masquelier, *Nat. Mater.* **2019**, 18, 1278.
- [22] A. S. Westover, N. J. Dudney, R. L. Sacci, S. Kalnaus, *ACS Energy Lett.* **2019**, 4, 651.
- [23] R. W. Johnson, A. Hultqvist, S. F. Bent, *Mater. Today* **2014**, 17, 236.
- [24] P. Yan, J. Zheng, J. Liu, B. Wang, X. Cheng, Y. Zhang, X. Sun, C. Wang, J.-G. Zhang, *Nat. Energy* **2018**, 3, 600.
- [25] B. Wang, J. Liu, Q. Sun, R. Li, T.-K. Sham, X. Sun, *Nanotechnology* **2014**, 25, 504007.
- [26] a) N. D. Lepley, N. A. W. Holzwarth, Y. A. Du, *Phys. Rev. B* **2013**, 88, 104103; b) L. D. Prayogi, M. Faisal, E. Kartini, W. Honggowiranto, Supardi, *AIP Conf. Proc.* **2016**, 1708, 030047; c) L. Wang, Q. Wang, W. Jia, S. Chen, P. Gao, J. Li, *J. Power Sources* **2017**, 342, 175; d) H. Guo, G. Hou, J. Guo, X. Ren, X. Ma, L. Dai, S. Guo, J. Lou, J. Feng, L. Zhang, P. Si, L. Ci, *ACS Appl. Energy Mater.* **2018**, 1, 5511.
- [27] C. Monroe, J. Newman, *J. Electrochem. Soc.* **2005**, 152, A396.
- [28] Y. Wang, P. Yan, J. Xiao, X. Lu, J.-G. Zhang, V. L. Sprenkle, *Solid State Ionics* **2016**, 294, 108.
- [29] Y. Wang, W. Lai, *J. Power Sources* **2015**, 275, 612.
- [30] Y. Li, J.-T. Han, C.-A. Wang, H. Xie, J. B. Goodenough, *J. Mater. Chem.* **2012**, 22, 15357.
- [31] K. Kerman, A. Luntz, V. Viswanathan, Y.-M. Chiang, Z. Chen, *J. Electrochem. Soc.* **2017**, 164, A1731.
- [32] J. Kasemchainan, S. Zekoll, D. Spencer Jolly, Z. Ning, G. O. Hartley, J. Marrow, P. G. Bruce, *Nat. Mater.* **2019**, 18, 1105.
- [33] Y. Zhu, J. G. Connell, S. Tepavcevic, P. Zapol, R. Garcia-Mendez, N. J. Taylor, J. Sakamoto, B. J. Ingram, L. A. Curtiss, J. W. Freeland, D. D. Fong, N. M. Markovic, *Adv. Energy Mater.* **2019**, 9, 1803440.
- [34] F. Han, Y. Zhu, X. He, Y. Mo, C. Wang, *Adv. Energy Mater.* **2016**, 6, 1501590.
- [35] X. Zhang, T. Liu, S. Zhang, X. Huang, B. Xu, Y. Lin, B. Xu, L. Li, C.-W. Nan, Y. Shen, *J. Am. Chem. Soc.* **2017**, 139, 13779.
- [36] M. Wang, J. Sakamoto, *J. Power Sources* **2018**, 377, 7.